On specimen design for size effect evaluation in ultrasonic gigacycle fatigue testing

**Please cite this article as:**

"PAOLINO, D.S., TRIDELLO, A., CHIANDUSSI, G. and ROSSETTO, M. (2014). On specimen design for size effect evaluation in ultrasonic gigacycle fatigue testing. *Fatigue and Fracture of Engineering Materials and Structures* doi:10.1111/ffe.12149."

**On specimen design for size effect evaluation in ultrasonic gigacycle fatigue testing**

**Authors:**
D.S. Paolino[a], A. Tridello[b], G. Chiandussi[c], M. Rossetto[d]

[a] Department of Mechanical and Aerospace Engineering, Politecnico di Torino, 10129 Turin, Italy, davide.paolino@polito.it
[b] Department of Mechanical and Aerospace Engineering, Politecnico di Torino, 10129 Turin, Italy, andrea.tridello@polito.it
[c] Department of Mechanical and Aerospace Engineering, Politecnico di Torino, 10129 Turin, Italy, giorgio.chiandussi@polito.it
[d] Department of Mechanical and Aerospace Engineering, Politecnico di Torino, 10129 Turin, Italy, massimo.rossetto@polito.it

**Corresponding Author:**
D.S. Paolino
*E-mail address*: davide.paolino@polito.it
*Full postal address*:
C.so Duca degli Abruzzi 24,
Department of Mechanical and Aerospace Engineering – Politecnico di Torino,
10129 – Turin,
ITALY
*Phone number*: +39.011.090.5746
*Fax number*: +39.011.090.6999

**Abstract:**

Literature datasets showed that gigacycle fatigue properties of materials may be affected by the specimen risk-volume, i.e. the part of the specimen subjected to stress amplitudes above a prescribed percentage of the maximum stress. The paper proposes a Gaussian specimen shape able to attain large risk-volumes for gigacycle fatigue tests, together with a general procedure for its design: wave propagation equations are analytically solved in order to obtain a specimen shape characterized by a uniform stress distribution on an extended length and, as a consequence, by a larger risk-volume. The uniformity of the stress distribution in the Gaussian specimen is numerically verified through a finite element analysis and experimentally validated by means of strain gage measurements.

**Keywords:**

Very-high-cycle fatigue; Ultra-high-cycle fatigue; Ultrasonic testing machine; Risk-volume; Wave propagation equations

**Nomenclature**

$A, B, A_1, B_1, A_2, B_2, a, b, c, S_0 =$ constant coefficients
$D_1, D_2 =$ characteristic diameters of the specimen
$d_3(\cdot) =$ diameter function in specimen part 3
$E_d =$ dynamic Young's modulus
$\mathrm{erf}(\cdot) =$ error function
$f_0 =$ resonance frequency
$K_t =$ stress concentration factor
$k =$ wave number
$L_1, L_2, L_3 =$ characteristic lengths of the specimen
$M_\sigma =$ stress amplification factor
$N =$ diameter ratio
$\upsilon =$ Poisson's ratio
$\rho =$ density
$s(\cdot) =$ cross-section function
$\sigma(\cdot) =$ stress amplitude function
$\sigma, \sigma_1, \sigma_{center}, \sigma_{max,long,3}, \sigma_{max,overall} =$ characteristic stress values
$U_{in} =$ displacement amplitude at the interface between horn and specimen
$u(\cdot), u_1(\cdot), u_2(\cdot), u_3(\cdot) =$ displacement amplitude functions
$V =$ theoretical volume with constant stress amplitude
$z =$ longitudinal coordinate of the specimen

## 1. Introduction

In recent years, the interest in very-high-cycle fatigue (VHCF) behavior of metallic materials is significantly increased. Design requirements in specific industrial fields (aerospace, mechanical and energy industry) for structural components characterized by even larger fatigue lives, up to $10^{10}$ cycles (gigacycle region), lead to a more detailed investigation on material properties in the gigacycle region.

Gigacycle fatigue tests are commonly performed using resonance fatigue testing machines (see [1] and [2] for an updated review) with a loading frequency of $20\ \mathrm{kHz}$ (ultrasonic tests). Experimental results show that failure is due to cracks which nucleate at the specimen surface if the stress amplitude is above the conventional fatigue limit (surface nucleation) and that failure is generally due to cracks which nucleate from inclusions or internal defects (internal nucleation) when specimens are subjected to stress amplitudes below the conventional fatigue limit.

In the gigacycle region, several factors (e.g., load type [3], stress ratio [4,5], surface finishing [6], environment [7]) were found to significantly influence the fatigue strength of metallic materials. The effect of the specimen size on the fatigue strength was recently investigated by Furuya [8-10]. The experimental results in [8-10] seem to disagree with previous studies carried out by Bathias (see pp. 97 and 105 in [1]) on hourglass specimens with different minimum diameters (i.e., with different sizes), made of spring steel or spheroidal graphite cast iron. In particular, differently from what showed by Bathias (i.e., no significant difference exists between specimens with different sizes), Furuya [8-10] found that, in high strength steel, the fatigue strength strongly decreases when the specimen size significantly increases: he finally concluded that "*using small specimens is very dangerous, since they are likely to show misleadingly high VHCF strength*" [10]. The decrement in fatigue strength was physically justified by Furuya [10] considering that the larger the risk-volume (region subjected to a stress amplitude above the 90% of the maximum stress amplitude [8]), the larger the probability of finding inclusions causing failure. In order to increase the risk-volume of the hourglass-shaped specimens commonly used for gigacycle fatigue tests (about $33\ \mathrm{mm}^3$), Furuya [8-10] adopted dog-bone shaped specimens characterized by large risk-volumes (about $900\ \mathrm{mm}^3$). In this respect, the different results found in the literature on the influence of the size effect require further investigation: the experimental results showed in [1] are obtained by testing hourglass specimens with a limited increment in the risk-volume; in [8-10] the size effect is more relevant, since the studied range of variation of the risk-volume is significantly larger. Therefore, it would be extremely interesting to further increase the investigated range of variation of the risk-volume. However, due to the non-uniform stress distribution along the specimen part with constant cross section, a further increment of the risk-volume remains extremely limited with dog-bone shaped specimens.

The present paper proposes a specimen shape (*Gaussian specimen*) able to attain larger risk-volumes for gigacycle fatigue tests, together with a general procedure for its design: wave propagation equations are analytically solved in order to obtain a specimen shape characterized by a uniform stress distribution on an extended length and, as a consequence, by a larger risk-volume.

The stress distribution along the specimen profile is verified through a Finite Element Analysis (FEA) and validated experimentally through strain gage measurements. Given the same theoretical risk-volume, a dog-bone shaped specimen and a Gaussian specimen are also designed and compared.

**2. Specimen shape with uniform stress distribution**

Specimens for ultrasonic tests are obtained on the basis of the equations for wave propagation in an elastic solid. In deriving the basic design relationships, the specimen is modeled as a one dimension linear elastic body: stresses are considered as uniformly distributed on the cross section and transverse displacements are considered as negligible if compared to longitudinal displacements. In case of a specimen with variable cross-section, according to these assumptions, the displacement amplitude along the specimen $u(z)$ can be obtained by solving the Webster's equation for a plane wave:

$$u''(z) + \frac{s'(z)}{s(z)}u'(z) + k^2u(z) = 0, (1)$$

where $u''(z) = d^2u(z)/dz^2$, $s(z)$ is the specimen cross-section, $s'(z) = ds(z)/dz$, $u'(z) = du(z)/dz$ and $k = 2\pi f_0/\sqrt{E_d/\rho}$ is the wave number, being $f_0$ the resonance frequency, $\rho$ the specimen density and $E_d$ the dynamic elastic modulus of the specimen. It is worth noting that, for a constant cross-section specimen (i.e., $s'(z) = 0$), Equation (1) simplifies significantly and can be easily satisfied by considering a sinusoidal displacement distribution (see Appendix A).

By applying an inverse design procedure (see e.g., [11,12]), the specimen cross-section which assures an imposed displacement distribution is given by:

$$s(z) = S_0 \cdot e^{-\int \frac{k^2u(z)+u''(z)}{u'(z)}dz}, (2)$$

where $S_0$ is a constant of integration whose value depends on the boundary conditions. For a linear elastic body, according to the kinematic equations, the stress distribution $\sigma(z)$ is given by $\sigma(z) = E_d u'(z)$. Since $\sigma(z)$ is proportional to $u'(z)$, a linear displacement distribution has to be taken into consideration in order to obtain a uniform stress distribution:

$$u(z) = A(k \cdot z) + B, (3)$$

where $A$ and $B$ are constant coefficients that depend on the boundary conditions. With easy passages and by taking into account Equation (3), Equation (2) becomes:

$$s(z) = a \cdot e^{-\frac{(z-b)^2}{2c^2}}, \quad (4)$$

being $a = S_0 \cdot e^{\frac{B^2}{2A^2}}$, $b = -\frac{B}{kA}$ and $c = k^{-1}$.

According to Equation (4), the specimen cross-section able to provide a uniform stress distribution for different values of $z$ entails the typical Gaussian form [11,12] with parameters $a$, $b$ and $c$. Since [11], resonant vibrators with a Gaussian shape are commonly considered in the literature (see e.g.,

[12] and, more recently, [13]) as concentrators or horns aiming at amplifying the vibration amplitude while limiting and controlling the stress amplitude. The Gaussian resonant vibrators proposed in this paper are originally conceived as risk-volume amplifiers characterized by a full Gaussian form which differs from the vibrator ampullaceus commonly considered in the literature.

In order to completely define the Gaussian specimen cross-section, the values of the parameters $a$, $b$ and $c$ in Equation (4) must be determined. For a given specimen material and resonance frequency, the $k$ value and, as a consequence, the parameter $c$ can be easily computed. As for the parameters $a$ and $b$, it is necessary to determine the value of the ratio $B/A$ and the value of the integration constant $S_0$. These values can be obtained by imposing proper boundary conditions for the displacement distribution.

In particular, let $u_3(z)$ denote the displacement amplitude along the Gaussian shaped part of the specimen (part 3 in Figure 1).

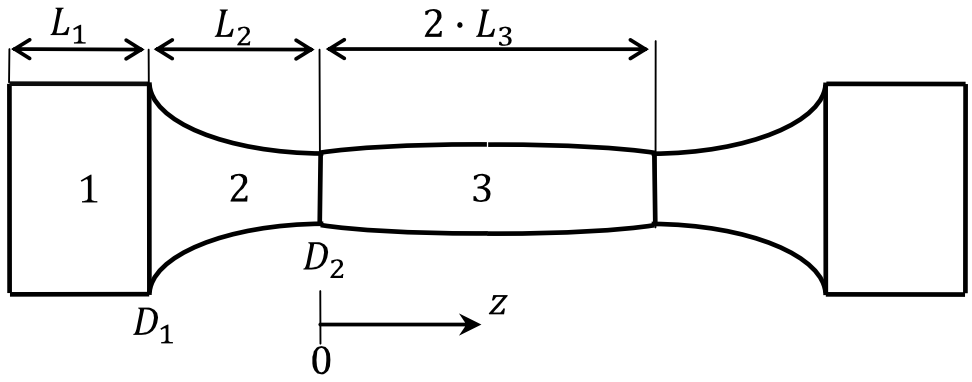


Figure 1: Geometry of a Gaussian specimen and its subdivision in parts.

Due to symmetry, the condition $u_3(L_3) = 0$ must be fulfilled, being $L_3$ half of the total length of specimen part 3. By taking into account Equation (3), the symmetry condition yields:

$$B/A = -kL_3. \quad (5)$$

By substituting Equation (5) in Equation (4), the cross-section of specimen part 3, $s_3(z)$, can be finally expressed as follows:

$$s_3(z) = S_0 \cdot e^{\left(\frac{kL_3}{\sqrt{2}}\right)^2} e^{-\left(\frac{k(z-L_3)}{\sqrt{2}}\right)^2}. \quad (6)$$

Equation (6) can be used to evaluate the variation of the cross-section area depending on the longitudinal coordinate $z$, being $0 \leq z \leq L_3$. In particular, for $z = 0$, Equation (6) gives $s_3(0) = S_0$. By taking into account Equation (6) and the diameter corresponding to $s_3(0)$ (i.e., $D_2$ in Figure 1), the cross-section diameter $d_3(z)$ along part 3 of the specimen can be easily obtained:

$$d_3(z) = D_2 \cdot e^{\left(\frac{kL_3}{2}\right)^2} e^{-\left(\frac{k(z-L_3)}{2}\right)^2}. \quad (7)$$

The total volume $V$ of the Gaussian part of the specimen can be computed by integrating Equation (6) with respect to $z$ from 0 to $2L_3$:

$$V = \int_0^{2L_3} s_3(z)dz = \frac{D_2^2}{k}\left(\frac{\pi}{2}\right)^{3/2} e^{\left(\frac{kL_3}{\sqrt{2}}\right)^2} \operatorname{erf}\left(\frac{kL_3}{\sqrt{2}}\right), \qquad (8)$$

where $\operatorname{erf}(\cdot)$ denotes the Error Function (i.e., $\operatorname{erf}(x) = \frac{2}{\sqrt{\pi}}\int_0^x e^{-t^2}dt$).

Once the wave number $k$ and the diameter $D_2$ are defined, Equation (8) allows to compute the length $L_3$ that provides the desired volume with a theoretical uniform stress distribution (i.e., the theoretical risk-volume). Figure 2 shows the variation of the non-dimensional parameter $kV/D_2^2$ with respect to the non-dimensional variable $kL_3$.

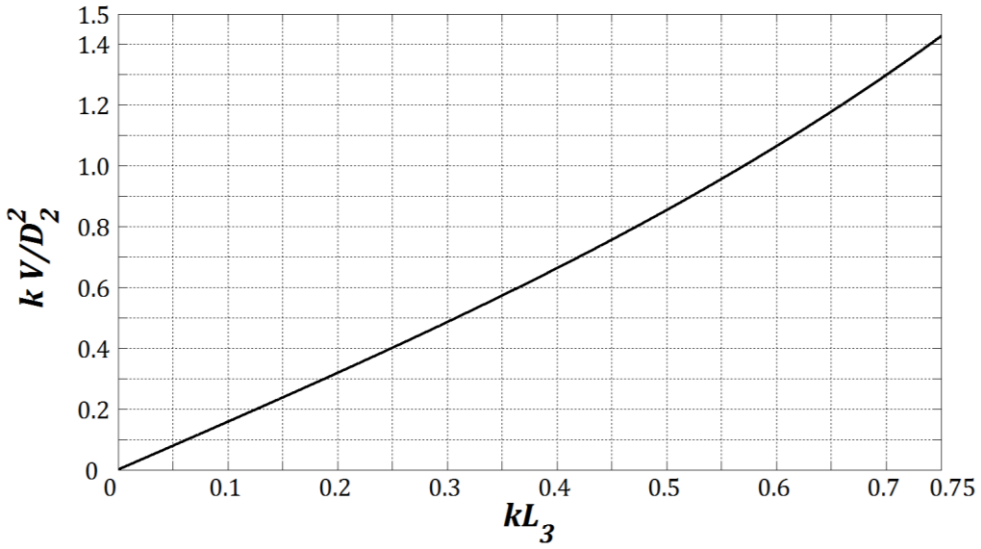


Figure 2: Plot of the parameter $kV/D_2^2$ vs. $kL_3$.

Figure 2 can also be used for a rapid graphical estimation of the specimen length $L_3$ corresponding to a theoretical risk-volume equal to $V$.

### 3. Gaussian specimen: overall design

Once $D_2$ and $L_3$ are determined according to Section 2, part 3 of the specimen (Figure 1) is completely defined. In order to design part 1 and part 2 of the specimen (Figure 1), the following boundary conditions must be imposed:

- the displacement at the interface between the horn and the specimen (i.e., at $z = -(L_1 + L_2)$ in Figure 1) is maximum (or minimum) and equal to $U_{in}$:

$$\begin{cases} u_1\big(-(L_1 + L_2)\big) = U_{in} \\ u_1'\big(-(L_1 + L_2)\big) = 0 \end{cases}, \qquad (9a)$$

  where $u_1(\cdot)$ and $u_1'(\cdot)$ denote the displacement and strain amplitude in the cylindrical specimen part (part 1 in Figure 1);

- displacement and strain have to be continuous at the interface between part 1 and part 2 of the specimen (i.e., at $z = -L_2$ in Figure 1):

$$\begin{cases} u_1(-L_2) = u_2(-L_2) \\ u_1'(-L_2) = u_2'(-L_2)' \end{cases} \qquad (9b)$$

  where $u_2(\cdot)$ and $u_2'(\cdot)$ denote the displacement and strain amplitudes in the catenoidal specimen part [1] (part 2 in Figure 1);

- displacement and strain have to be continuous at the interface between part 2 and part 3 of the specimen (i.e., at $z = 0$):

$$\begin{cases} u_2(0) = u_3(0) \\ u_2'(0) = u_3'(0) \end{cases}. \qquad (9c)$$

A further boundary condition has to be taken into account concerning the required stress amplitude in the risk-volume. Let define the stress amplification factor of the specimen, $M_\sigma$, as the ratio between the maximum stress amplitude $\sigma$ in part 3 of the specimen and the maximum stress amplitude $\sigma_1$ attainable in a cylindrical specimen with diameter equal to $D_1$ (part 1 in Figure 1), wave number equal to $k$ and initial displacement equal to $U_{in}$ (see [1]). The stress amplification factor can be expressed as:

$$M_\sigma = \frac{\sigma}{\sigma_1} = \frac{\sigma}{kU_{in}E_d} = A/U_{in}, \quad (10)$$

where, according to Equation (3) and by taking into account the assumption of linear elasticity, the stress amplitude in part 3 of the specimen is uniform and equal to the product $kAE_d$, while the maximum stress amplitude $\sigma_1$ is equal to the product $kU_{in}E_d$ (see [1]).

According to the boundary conditions described by Equations (9), the stress amplification factor of the specimen can also be described as (see Appendix 1):

$$M_\sigma = \left| N(\beta/k)\cos(kL_1)\left(\frac{\cos(\beta L_2)+\tan(\beta L_2)\sin(\beta L_2)}{\tan(\beta L_2)+(\beta/k)(kL_3)}\right)\right|, \qquad (11)$$

where $N = D_1/D_2$, $\beta = \sqrt{(kL_2)^2 - \operatorname{acosh}^2(N)}/L_2$ and:

$$kL_1 = \operatorname{atan}\left(-\left(\frac{(\beta/k)(kL_3)\tan(\beta L_2)-1}{\tan(\beta L_2)/(\beta/k)+(kL_3)} + \frac{\operatorname{acosh}(N)}{kL_2}\sqrt{1-N^{-2}}\right)\right). \qquad (12)$$

According to Equations (11) and (12), for a given value of $kL_3$, both $M_\sigma$ and $kL_1$ depend on the diameter ratio $N$ and on the non-dimensional variable $kL_2$. As a consequence, once part 3 of the specimen (see Section 2), the value of the initial displacement $U_{in}$, the desired maximum stress amplitude $\sigma$ and the diameter value $D_1$ have been defined, part 1 and part 2 of the specimen can be completely attained.

Figure 3 shows the variation of $M_\sigma = \sigma/(kU_{in}E_d)$ and $kL_1$ with respect to $kL_2$ for different diameter ratios, $N$ (each graph has been obtained for a specific value of $kL_3$).

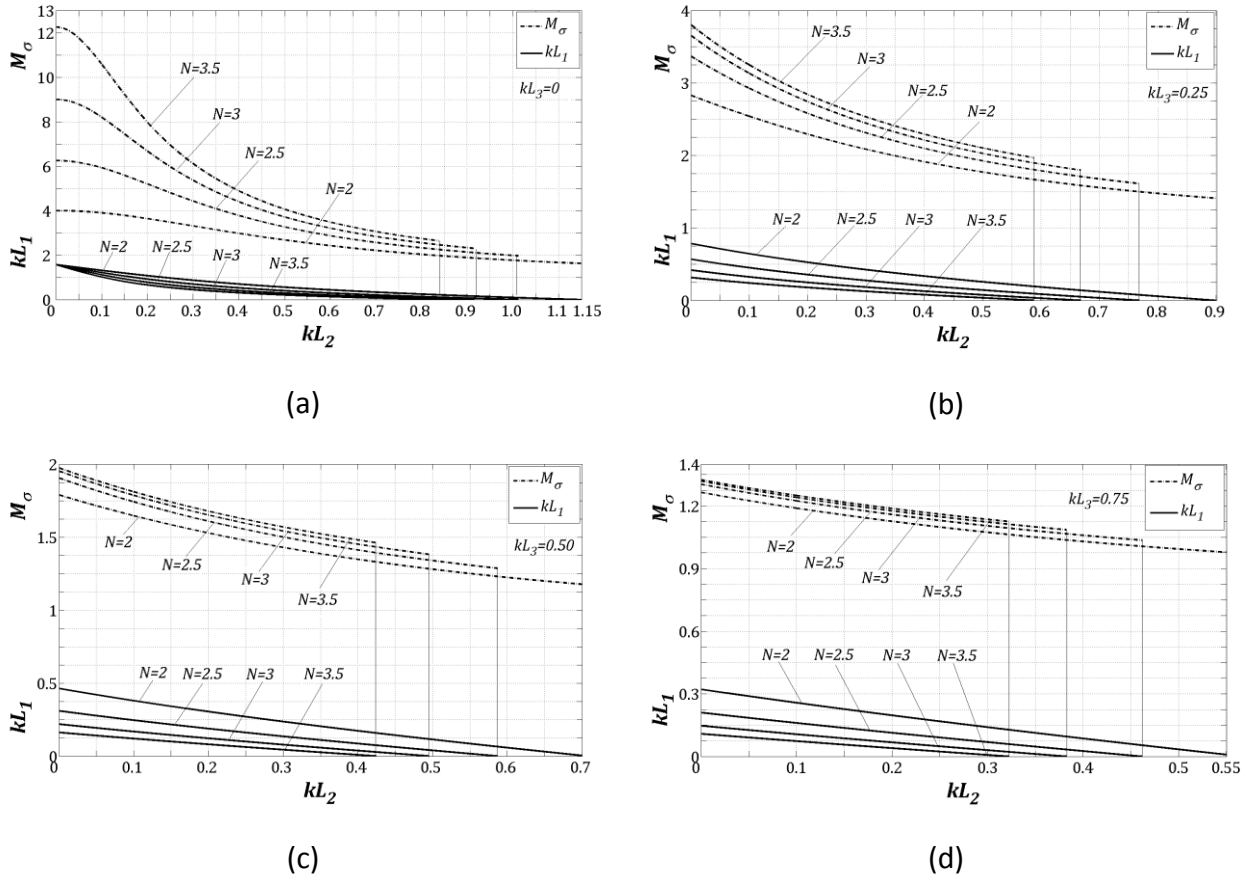


Figure 3: Plots of $M_\sigma$ and $kL_1$ vs. $kL_2$ for different values of $kL_3$: (a) $kL_3 = 0$ (hourglass specimen); (b) $kL_3 = 0.25$; (c) $kL_3 = 0.50$; (d) $kL_3 = 0.75$.

Figure 3 can be used for a quick graphical estimation of the lengths $L_2$ and $L_1$.

## 4. Illustrative example

The procedure proposed in Sections 2 and 3 is used to design a Gaussian specimen with a large theoretical risk-volume (Section 4.1). The stress distribution along part 3 of the designed Gaussian specimen is verified through a FEA (Section 4.2) and validated experimentally by means of strain gage measurements (Section 4.3). A dog-bone shaped specimen with the same theoretical risk-volume is also analyzed in order to compare the stress distributions in the central specimen parts.

### 4.1. Analytical design procedure

A steel specimen ($E_d = 206\,\text{GPa}$, $\upsilon = 0.29$ and $\rho = 7800\ \text{kg/m}^3$) with diameter $D_2$ equal to $10\ \text{mm}$ and theoretical risk-volume $V$ equal to $5000\ \text{mm}^3$ is considered for the analytical design procedure. The resonance frequency is set equal to the resonance frequency of the piezoelectric transducer ($20\ \text{kHz}$). As a consequence, the wave number $k$ is equal to $24.45\ \text{rad/m}$.

Given $V$, $k$ and $D_2$, Equation (8) permits to compute the length $L_3$: $L_3 = 27.4\ \text{mm}$.

According to Equation (10), given the initial displacement ($U_{in} = 33\ \mu\text{m}$), a stress amplification factor $M_\sigma$ equal to $1.2$ must be guaranteed in order to obtain a desired maximum stress amplitude $\sigma$ equal to $200\ \text{MPa}$.

For a diameter ratio $N$ equal to $2$ (i.e., $D_1 = 20\ \text{mm}$) and for given values of $L_3$ and $M_\sigma$, Equation (11) can be solved in order to obtain the length $L_2$: $L_2 = 10.1\ \text{mm}$.

Finally, length $L_1$ can be obtained from Equation (12): $L_1 = 8.0\ \text{mm}$.

The same specimen geometry can be defined through a graphical procedure (Figures 2 and 3). Given $V$, $k$ and $D_2$, the non-dimensional parameter $kV/D_2^2$ is equal to $1.22$. The corresponding value of $kL_3$ is $0.67$ (Figure 2), yielding to $L_3 = 27.4\ \text{mm}$. Given the amplification factor $M_\sigma = 1.2$, two values of the non-dimensional variable $kL_2$ can be obtained through the graphs in Figure 3 with $kL_3 = 0.5$ and $kL_3 = 0.75$. A linear interpolation allows to determine the value of $kL_2 = 0.26$ corresponding to $kL_3 = 0.67$. The estimated value of $kL_2$ yields $L_2 = 10.6\ \text{mm}$. Given $kL_2$, the same procedure can be repeated in order to obtain $kL_1$. The final estimated value of $kL_1$ is $0.19$ which yields $L_1 = 7.8\ \text{mm}$.

The approximated result is a consequence of the approximated evaluation of $kL_1$ and $kL_2$ through linear interpolation. Anyway, it has been verified that the geometrical errors due to the interpolation process have been verified and are generally characterized by a relative error smaller than 5%.

### 4.2. Finite element analysis

In order to verify the uniformity of the stress distribution in a Gaussian specimen along its central part (part 3 in Figure 1) at the first longitudinal frequency, the specimen geometry identified in Section 4.1 is used to create a numerical model for a modal FEA. The stress distribution along the specimen is also compared to that obtained by considering a dog-bone shaped specimen with the same theoretical risk-volume, wave number and diameters $D_1$ and $D_2$.

The numerical analyses are carried out by using the commercial FEA program ANSYS. Half of the geometric specimen model is considered due to its symmetry and eight-node quadrilateral elements (plane 82) with the axisymmetric option are used for the FEA. The numerical models count for 18630 elements for the dog-bone shaped specimen and for 16800 elements for the Gaussian specimen. The same material properties ($E_d$, $\upsilon$ and $\rho$) introduced in Section 4.1 are considered for both numerical specimen models.

Figure 4 shows the variation of the non-dimensional stress amplitude (stress amplitude normalized by the maximum stress value $\sigma_{max,long,3}$ reached along the longitudinal axis in part 3 of the specimen) with respect to the non-dimensional coordinate $z/L_3$. According to the definition of risk-volume considered in [8-10], a non-dimensional stress amplitude variation of 0.1 (dash-dot line in Figure 4) represents a possible tolerance limit for assuming the stress amplitude to be risky for crack nucleation.

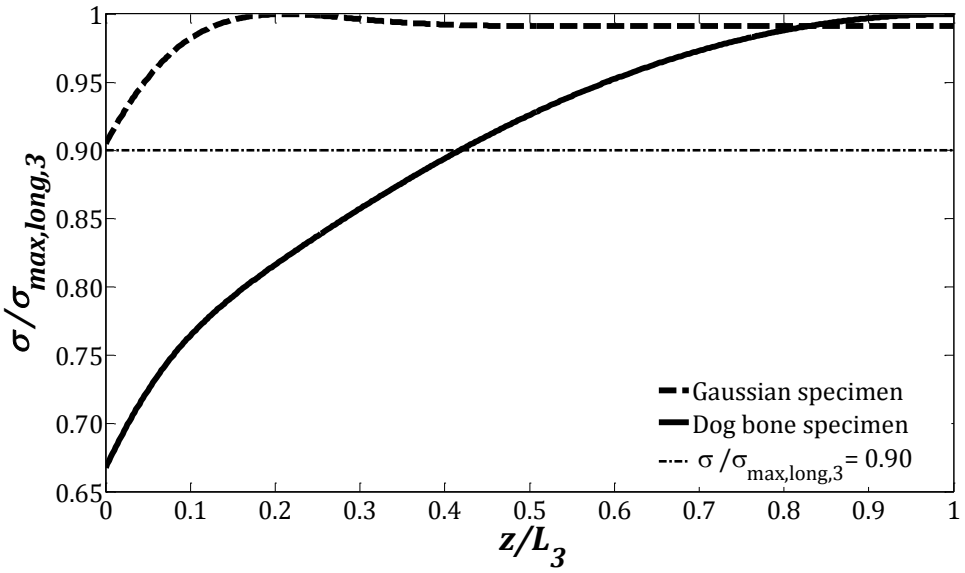


Figure 4: Stress distribution in central specimen part (numerical results) along the longitudinal axis.

According to Figure 4 and considering the Gaussian specimen, the stress amplitude along the longitudinal axis is larger than the 90% of $\sigma_{max,long,3}$ for the 100% of $L_3$ (corresponding to an actual risk-volume equal to 97% of the theoretical risk-volume). As for the dog-bone shaped specimen, the stress amplitude along the longitudinal axis is larger than the 90% of $\sigma_{max,long,3}$ for about the 60% of $L_3$ (corresponding to an actual risk-volume equal to 58% of the theoretical risk-volume).

Finally, the variation of the longitudinal stress along the radial direction is also verified in the analysis. For both specimens, the maximum stress amplitude is reached in correspondence of the longitudinal axis. The stress amplitude decreases from the longitudinal axis to the surface of the specimens with a very limited variation: when the specimen mid-section is considered, FEA results show a 1.1% stress amplitude reduction for the Gaussian specimen and a 0.2% stress amplitude reduction for the dog-bone shaped specimen. It should be noted that the larger the diameter of the central part of the specimen, the larger the stress amplitude reduction along the radial direction. This effect obviously limits the maximum risk-volume attainable with a Gaussian specimen. Since this kind of limitation could be a significant drawback for the practical application of the Gaussian specimens, the consequences of the stress amplitude reduction on the maximum attainable risk-volume were investigated with a number of FEA. The results obtained with FEA showed that specimens with significantly large risk-volumes (up to $20000\ \mathrm{mm}^3$) can be designed, regardless of the stress amplitude variation along the radial direction (risk-volumes were computed by considering the stress amplitude variation along any direction in the specimen).

### 4.3. Experimental validation

The stress distribution along the central part of the specimens is validated through an experimental test. The dog-bone shaped and Gaussian specimens which have been designed in Section 4.1 are produced in AISI 1040 carbon steel. Three T-rosettes strain gages (HBM 1-XY31-1.5/350), each with two strain gages connected at half bridge, are used for the evaluation of strain values at the specimen surface. For both specimens, the rosettes are bonded along the central specimen part:

the first rosette is bonded at the specimen mid-section, the second rosette at the 70% of $L_3$ and the third rosette at the 85% of $L_3$. Figure 5 shows the specimens after the application of the rosettes.

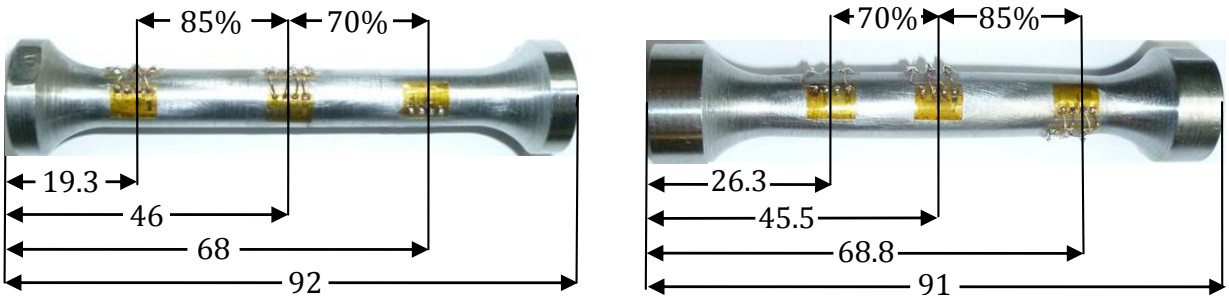


(a) (b)

Figure 5: Specimens after application of strain gage rosettes: (a) dog-bone shaped specimen; (b) Gaussian specimen.

A strain gage amplifier (EL-SGA-2/B by Elsys AG) is used for the completion of the Wheatstone bridge of each rosette and for the amplification of the signal. The measurement is acquired at a sample rate of $600$ kHz by a National Instruments data acquisition card (PCIe-6363).

An ultrasonic testing machine for fully reversed tension compression tests developed by the authors [14] is used for the test: specimens are subjected to load cycles for 3 seconds. Figures 6 and 7 show the strain measured at each point normalized by the value detected at the specimen mid-section, $\sigma_{center}$.

The acquired signals are fitted with a sine function (for each case, the correlation coefficient is larger than 99.99% and the mean value is equal to zero). As shown in Figures 6 and 7, the stress amplitude distribution is not uniform for the dog-bone shaped specimen while it is almost uniform for the Gaussian specimen.

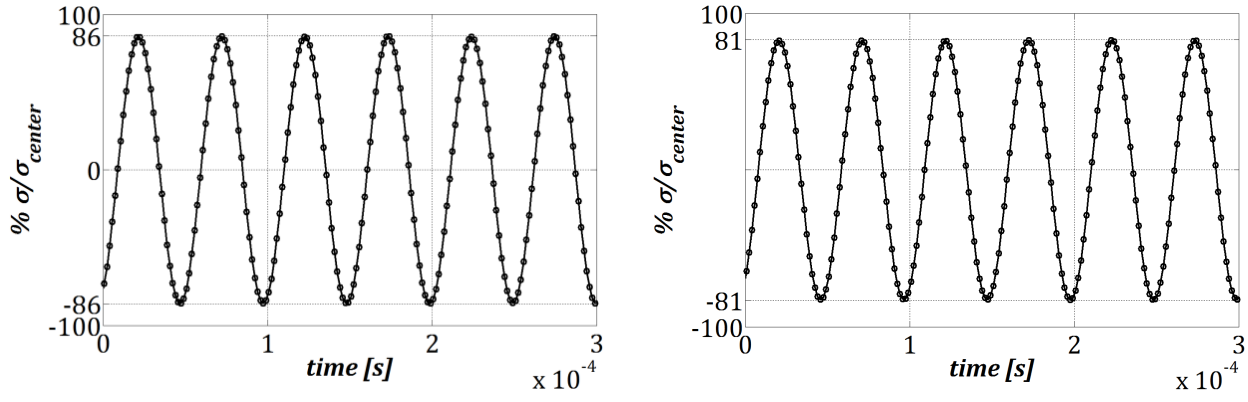


(a) (b)

Figure 6: Stress variation measured by strain gage rosettes bonded to the dog-bone shaped specimen: (a) rosette at 70% of $L_3$; (b) rosette at 85% of $L_3$.

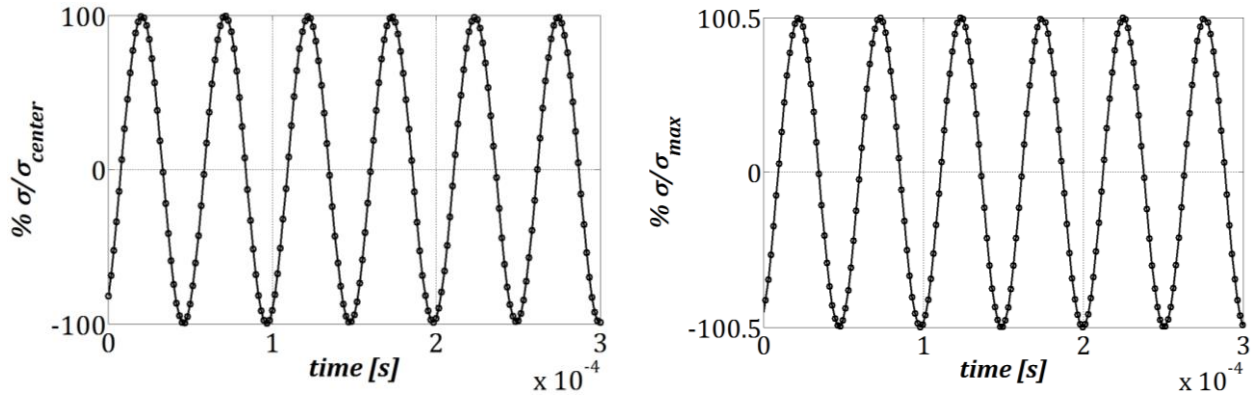


(a) (b)

Figure 7: Stress variation measured by strain gage rosettes bonded to the Gaussian specimen: (a) rosette at 70% of $L_3$; (b) rosette at 85% of $L_3$.

In particular, Table 1 reports a comparison between the stress variation obtained with the FEA and the experimental test.

Table 1: Comparison between numerical and experimental results: values of the $\sigma/\sigma_{center}$ percent ratio.

| **Analysis type** | $z/L_3 = 70$ % | | $z/L_3 = 85$ % | |
|---|---|---|---|---|
| | *Dog-bone* | *Gaussian* | *Dog-bone* | *Gaussian* |
| Finite Element | 85.8 % | 100. 0% | 80.2 % | 100.2 % |
| Experimental (95 % confidence interval) | [85.4; 86.5] % | [99.6; 100.8] % | [80.1; 81.4] % | [100.0; 101.1] % |

Note: Confidence intervals are obtained from 180 tests; for each experimental test, the stress amplitude is evaluated with a minimum of 1000 data points.

According to Table 1, the FEA results are included in the experimental confidence intervals. Therefore, it can be concluded that no significant statistical difference exists between FEA and experimental results. It is worth to note that, for the Gaussian specimen, the values larger than the 100% indicate a maximum stress amplitude not reached at the specimen mid-section (Figure 4).

## 5. Discussion

The numerical simulation and the experimental validation have raised some points of discussion which are dealt with in the following sub-sections.

### 5.1. Stress concentration

A stress concentration is present at the interface between part 2 and part 3 of the specimen ($z = 0$ in Figure 1), even though an appropriate fillet radius is adopted. In order to evaluate the stress concentration effects, the stress concentration factor $K_t$ is conservatively considered in place of the fatigue strength reduction factor $K_f$. The $K_t$ value is computed as the ratio between the overall

maximum stress (i.e., $\sigma_{max,overall}$) reached in the specimen and the maximum stress reached along the longitudinal axis in part 3 of the specimen (i.e., $\sigma_{max,long,3}$):

$$K_t = \frac{\sigma_{max,overall}}{\sigma_{max,long,3}}. \qquad (13)$$

The experimental results shown in [8] demonstrate that no failure occurs in the region affected by the stress concentration, even if the $K_t$ value is equal to $1.08$. Therefore, it could be concluded that, according to the experimental data in [8], the stress concentration effects does not influence the experimental results if $K_t$ is limited to $1.08$.

It is possible to obtain Gaussian specimens with $K_t$ smaller or equal to $1.08$ if the diameter ratio $N$ is properly chosen. For this purpose, the design procedure described in Sections 2 and 3 has to be iteratively carried out by varying the diameter ratio until a specimen with the desired amplification factor, risk-volume and stress concentration factor is obtained. As an example, if the specimen designed in Section 4 is taken into consideration, the FEA allows to calculate a stress concentration factor $K_t = 1.12$, slightly larger than $1.08$. A smaller $K_t$ value ($K_t = 1.06$) can be obtained if the diameter ratio $N$ is reduced to $1.6$ by increasing the diameter $D_2$ (see [15]).

**5.2. Practical application of Gaussian specimens**

It is generally acknowledged that planar acoustic waves assumed in Equation (1) are appropriate if specimens with smooth changes of the diameter are calculated. Indeed, local stress variations due to stress concentrations effects and radial stress variations cannot be considered with Equation (1) and they must be estimated through FEA. However, it is worth noting that results reported in the experimental validation showed that the errors in the overall design of the specimens are negligible even if the changes of diameter are not smooth (see e.g., part 2 of the specimen) and the radial dimension is not small if compared to the longitudinal dimension: in the Gaussian specimen case, the resonance frequency computed with FEA is 0.35% smaller than the theoretical one and the actual risk-volume is only 3% smaller than the theoretical one. In this respect, the analytical approach can be properly adopted in practical design of Gaussian specimens.
It should also be noted that the effects of shape errors on the resonance frequency of the specimen must be taken into account for the practical application of Gaussian specimens. In this respect, in [16], the Authors analyzed the substitution of the Gaussian profile (part 3 of the specimen in Figure 1) with an arc-of-circle. FEA results reported in [16] show that the profile modification induces negligible effects both on the resonance frequency and on the final risk-volume of the specimen.

Some other aspects need to be considered when designing a Gaussian specimen characterized by a long Gaussian part. In particular, an increment of the length of the Gaussian specimen part generally reduces the stress amplification factor. As a consequence, in order to obtain the same stress amplitude in the Gaussian specimen part, the vibration amplitude and the absorbed power of the ultrasonic converter must significantly increase.

As for the vibration amplitude, by designing ultrasonic horns with the desired amplification factor it is possible to reach maximum displacement amplitudes larger than $100\ \mu\text{m}$. The ultrasonic system

(piezoelectric converter, booster and catenoidal horn with amplification factor equal to 4) adopted for the experimental validation [14] can reach up to $110\ \mu m$ with a maximum stress amplitude in the horn smaller than $120\ MPa$. If the Gaussian specimen considered for the experimental validation is excited by a vibration amplitude equal to $110\ \mu m$, the stress amplitude in the Gaussian specimen part reaches about $660\ MPa$, a value slightly larger than the maximum fatigue strength ($620\ MPa$) obtain by Furuya in [8-10] for different high-strength steel specimens with maximum risk-volume equal to $912\ mm^3$. However, it is worth noting that, according to the experimental results in [9], if the risk-volume increases from $254\ mm^3$ to $780\ mm^3$ (i.e., about 3 times larger than $254\ mm^3$) the percent fatigue strength decrement becomes equal to 18% (from about $680\ MPa$ to $560\ MPa$). Therefore, it can be expected that, for a risk-volume equal to $5000\ mm^3$ (i.e., about 6 times larger than $780\ mm^3$ and 5 times larger than $912\ mm^3$), the fatigue strength reduces to a value significantly smaller than $660\ MPa$ and, consequently, the experimental tests can be performed with a vibration amplitude significantly smaller than $110\ \mu m$. In this respect, it must be also considered that, since the distance between the transition stress (the stress differentiating surface and internal failure modes in a duplex *S-N* curve [17,18]) and the fatigue strength at a specific risk-volume increases with the risk-volume, for larger risk-volumes it is possible to accept larger stress concentration factors (which induce a surface failure mode) and, as a consequence, to increase the stress amplification factor of the specimen (see Figure 3). As a consequence, an increment of the stress amplification factor allows to further decrease the vibration amplitude that must be supplied by the ultrasonic system in case of gigacycle fatigue tests on specimens with large risk-volumes.

As for the power absorption, the experimental validation performed on the Gaussian specimen showed that, for a vibration amplitude equal to $33\ \mu m$ as measured at the free end of the specimen (laser displacement transducer Keyence type LK-G5000 with sensor head LK-H022), the absorbed power supplied by the generator is $18\ W$. Since, in case of hysteretic damping, the absorbed power is proportional to the square of the vibration amplitude, it can be expected that, for a maximum vibration amplitude equal to $110\ \mu m$, the maximum absorbed power is equal to about $200\ W$ (10% of the maximum power supplied by the generator adopted for the experimental validation). It must be noted that the hysteretic damping could induce a significant temperature increment, when large risk-volumes are to be tested, as in the case of the Gaussian specimens. In this respect, the temperature should be carefully controlled during the test and its increment should not prevent the proper execution of the ultrasonic test. For this reason, temperature was measured during the validation test performed on the Gaussian specimen. The test was performed in air at room temperature and the maximum temperature (measured with an infrared sensor OPTRIS CT-LT-15) reached on the surface of the Gaussian part of the specimen at the end of the load cycle (about 3 seconds) was smaller than $40\ °C$. The same increment was found when the load cycle was repeated after the cooling phase. However, it must be considered that such an increment was found when testing the specimen at a stress amplitude equal to $200\ MPa$. The temperature increment is expected to raise when testing at larger stress amplitudes. Further studies are needed in order to completely investigate the effect of the hysteretic damping in terms of specimen design and temperature increment.

Finally, when designing a Gaussian specimen, buckling effects must also be taken into consideration: indeed, the larger the length of the Gaussian specimen part, the smaller the critical buckling stress. As an example, by conservatively considering the Gaussian specimen part with a constant cross-section equal to $\pi D_2^2/4$ and a buckling length equal to $2.1 \cdot 2L_3$, the critical buckling stress of the Gaussian specimen considered for the experimental validation is $960\ \mathrm{MPa}$, a value significantly larger (i.e., not critical) than the maximum stress amplitude attainable with the ultrasonic system.

**6. Conclusions**

The proposed Gaussian shape allows to design specimens characterized by a very large range of risk-volume values. The analytical stress distribution along the Gaussian part of the specimen has been verified numerically by FEA and experimentally on an ultrasonic testing machine by using strain gages.

The analytical equations for designing Gaussian specimens are provided. Simplified plots for an easier and faster design of the specimens are also given. The numerical verification and the experimental validation showed that the simplistic hypotheses assumed for the analytical design of the specimen give raise to negligible design errors. The analytical design procedure can be thus properly adopted for practical applications.

The stress concentration effect due to the cross section variation along the specimen length has been taken into account. A design procedure has been proposed in order to obtain specimens with the same risk-volume and a $K_t$ value equal or even smaller than that of the traditional dog-bone shaped specimens.

Practical application of the Gaussian specimen in gigacycle fatigue test was discussed. Possible shape errors in the Gaussian profile are negligible both in terms of resonance frequency and in terms of final risk-volume of the specimen. The vibration amplitude and the power of ultrasonic converters, together with possible buckling effects were taken into account and were found to be not critical for the practical application of the Gaussian specimens. The temperature increment was also found to be moderate at small stress amplitudes. Further investigation is in progress, in order to evaluate the effects of the hysteretic damping on the specimen design as well as on the temperature increment during ultrasonic tests at large stress amplitudes.

**A1. Appendix 1: Proofs of Equations (11) and (12)**

According to Equation (10), the stress amplification factor of the specimen, $M_\sigma$, is equal to:

$$M_\sigma = A/U_{in}, \quad \text{(A1)}$$

where $A$ is a constant value depending on the boundary conditions and $U_{in}$ represents the displacement amplitude at the interface between the horn and the specimen. The value of $A$ in Equation (A1) can be determined by taking into account Equations (9) and the displacement amplitude in each specimen part [1]:

$$\begin{cases} u_1(z) = A_1\cos\Big(k\big(z+(L_1+L_2)\big)\Big) + B_1\sin\Big(k\big(z+(L_1+L_2)\big)\Big) \\ u_2(z) = \frac{A_2\cos\big(\beta(z+L_2)\big)+B_2\sin\big(\beta(z+L_2)\big)}{\cosh(z\cdot\operatorname{acosh}(N)/L_2)} \\ u_3(z) = Ak(z-L_3) \end{cases}, \quad \text{(A2)}$$

where $A_1$, $B_1$, $A_2$ and $B_2$ are constant values. $A_1$ and $B_1$ can be obtained from the boundary conditions concerning part 1 of the specimen (Equation 9a) and, as a consequence, $u_1(z)$ can be rewritten as:

$$u_1(z) = U_{in}\cos\Big(k\big(z+(L_1+L_2)\big)\Big). \quad \text{(A3)}$$

By considering Equations (9b) and (9c):

$$\begin{cases} u_1(-L_2) = u_2(-L_2) \\ u_2(0) = u_3(0) \end{cases}, \quad \text{(A4)}$$

and by taking into account Equations (A2) and (A3), constant $A$ can be expressed as:

$$A = -\frac{N}{\sqrt{1+(\tan(kL_1))^2}}\frac{U_{in}\big(\cos(\beta L_2)+B_2/A_2\sin(\beta L_2)\big)}{kL_3}. \quad \text{(A5)}$$

The ratio $B_2/A_2$ in Equation (A5) can be obtained by taking into account Equations (9c):

$$\frac{u_2(0)}{u_2'(0)} = \frac{u_3(0)}{u_3'(0)}. \quad \text{(A6)}$$

Equations (A2) and (A6) finally yield:

$$\frac{B_2}{A_2} = \frac{(\beta/k)(kL_3)\tan(\beta L_2)-1}{\tan(\beta L_2)+(\beta/k)(kL_3)}. \quad \text{(A7)}$$

By taking into consideration Equations (A1), (A5) and (A7), the stress amplification factor finally becomes:

$$M_\sigma = \left|N\frac{\beta/k}{\sqrt{1+(\tan(kL_1))^2}}\left(\frac{\cos(\beta L_2)+\tan(\beta L_2)\sin(\beta L_2)}{\tan(\beta L_2)+(\beta/k)(kL_3)}\right)\right|. \quad \text{(A8)}$$

Equation (A8) corresponds to Equation (11).

The product $kL_1$ in Equation (A8) can be obtained by taking into account Equations (9b):

$$\frac{u_1(-L_2)}{u_1'(-L_2)} = \frac{u_2(-L_2)}{u_2'(-L_2)}. \qquad \text{(A9)}$$

Equations (A2) and (A9) finally yield:

$$kL_1 = \operatorname{atan}\left(-\left(\frac{B_2}{A_2}\frac{\beta}{k} + \frac{\operatorname{acosh}(N)}{kL_2}\sqrt{1-N^{-2}}\right)\right), \qquad \text{(A10)}$$

which, if Equation (A7) is taken into consideration, corresponds to Equation (12).

**References**


1 Bathias, C., Paris, P.C. (2005) *Gigacycle fatigue in mechanical practice*. CRC Dekker, New York, USA.

2 Stanzl-Tschegg, S. (In press) Very high cycle fatigue measuring techniques. *Int. J. Fatigue*.

3 Akiniwa, Y., Stanzl-Tschegg, S., Mayer, H., Wakita, M., Tanaka, K. (2008) Fatigue strength of spring steel under axial and torsional loading in the very high cycle regime. *Int. J. Fatigue* **30**, 2057–2063.

4 Shiozawa, K., Hasegawa, T., Kashiwagi, Y., Lu, L. (2009) Very high cycle fatigue properties of bearing steel under axial loading condition. *Int. J. Fatigue* **31**, 880–888.

5 Sakai, T., Sato, Y., Nagano, Y., Takeda, M., Oguma, N. (2006) Effect of stress ratio on long life fatigue behavior of high carbon chromium bearing steel under axial loading. *Int. J. Fatigue* **28**, 1547–1554.

6 Itoga, H., Tokaji, K., Nakajima, M., Ko, H.-N. (2003) Effect of surface roughness on step-wise S–N characteristics in high strength steel. *Int. J. Fatigue.* **25**, 379–385.

7 Tokaji, K., Ko, H.-N., Nakajima, M., Itoga, H. (2003) Effects of humidity on crack initiation mechanism and associated S-N characteristics in very high strength steels. *Mater. Sci. Eng. A* **345**, 197–206.

8 Furuya, Y. (2008) Specimen size effects on gigacycle fatigue properties of high-strength steel under ultrasonic fatigue testing. *Scripta Mater.* **58**, 1014–1017.

9 Furuya, Y. (2010) Size effects in gigacycle fatigue of high-strength steel under ultrasonic fatigue testing. *Procedia Eng.* **2**, 485–490.

10 Furuya, Y. (2011) Notable size effects on very high cycle fatigue properties of high strength steel. *Mater. Sci. Eng. A* **528**, 5234–5240.

11 Kleesattel, C. (1962) Vibrator ampullaceus. *Acustica* **12**, 322-334.

12 Eisner, E., Seager, J.S. (1965) A longitudinal resonant stub for vibrations of large amplitude. *Ultrason.* **3**, 88–98.

13 Roopa Rani, M., Rudramoorthy, R. (2013) Computational modeling and experimental studies of the dynamic performance of ultrasonic horn profiles used in plastic welding. *Ultrason.* **53**, 763–772.

14 Paolino, D.S., Rossetto, M., Chiandussi, G., Tridello, A. (2012) *Sviluppo di una macchina a ultrasuoni per prove di fatica gigaciclica*. Proceedings of the 41$^{th}$ AIAS Conference, Vicenza, (In Italian).

15 Tridello, A., Paolino, D.S., Chiandussi, G., Rossetto, M. (2013) Comparison between dog-bone and Gaussian specimens for size effect evaluation in gigacycle fatigue. *Frattura e Integrità Strutturale* **26**, 49-56.

16 Tridello, A., Paolino, D.S., Chiandussi, G., Rossetto, M. (2014) Analytical design of gigacycle fatigue specimens for size effect evaluation. *Key Eng. Mater.* **577-578**, 369-372.

17 Paolino, D.S., Chiandussi, G., Rossetto, M. (2013) A unified statistical model for S-N fatigue curves: probabilistic definition. *Fatigue Fract. Eng. Mater. Struct.* **36**, 187-201.

18 Mughrabi, H. (2002) On 'multi-stage' fatigue life diagrams and the relevant life-controlling mechanisms in ultrahigh-cycle fatigue. *Fatigue Fract. Eng. Mater. Struct.* **25**, 755-764.